Impact of GdOx insertion on magnetic anisotropy and damping in double-barrier magnetic stacks

Junyeon Kim[1], Takayuki Nozaki[1], Jun Uzuhashi[2], Shingo Tamaru[1], Tomohiro Ichinose[1], Takao Ochiai[1], Tatsuya Yamamoto[1], Tadakatsu Ohkubo[2], Kay Yakushiji[1] and Shinji Yuasa[1]

[1]*Research Center for Emerging Computing Technologies, National Institute of Advanced Industrial Science and Technology (AIST), Tsukuba, Ibaraki 305-8568, Japan.*

[2]*Research Center for Magnetic and Spintronic Materials, National Institute for Materials Science (NIMS), Tsukuba, Ibaraki 305-0047, Japan.*

For the realization of high-performance spintronic devices, the development of novel magnetic materials/structures satisfying both large perpendicular magnetic anisotropy (PMA) and ultra-low Gilbert damping is strongly desired. Here we show that insertion of an ultrathin GdOx layer as a capping in double-barrier ultrathin magnetic stacks provides such a solution. The inserted GdOx capping layer prevents unintended intermixing among the magnetic layer (CoFeB) and oxide layers (MgO and MgFeO), suppressing the deterioration of both the PMA and the Gilbert damping. Remarkably, the variation in the effective oxygen doping rate of the GdOx layer strongly influences both the PMA and the Gilbert damping, likely affected by a change in the polarization of the orbital magnetic moment. As a result, the GdOx inserted stacks present considerable effective PMA values (maximum ~0.55 erg/cm^2), while simultaneously maintaining an ultra-low Gilbert damping (minimum ~1.68×10^{-3}) within the range of 1.0-1.5 nm CoFeB thicknesses. These results pave the way to realize practical spintronic devices by providing reliable magnetic structures for efficient spin manipulation.

junyeon.kimu@aist.go.jp

Introduction

Spintronic devices have a strong potential as computing devices for both conventional and non-conventional architectures due to their unique physical properties, including non-volatility, and a high-compatibility with complementary metal-oxide semiconductor (CMOS) devices[1-5]. This fact requests the realization of nanometer-size high-performance spintronic devices operated with low power-consumption. One way to deal with this issue is finding an excellent mechanism for spin manipulation, as shown in various studies on voltage-controlled magnetic anisotropy (VCMA)[6-10], spin transfer torque (STT)[11-14], spin-orbit torque (SOT)[15-17], and orbital torque (OT)[18-20]. The development of optimal magnetic structures/materials is another vital issue. Particularly, the concurrent achievement of large perpendicular magnetic anisotropy (PMA) and low Gilbert damping are the most representative goals in the material study[21]. The PMA is a measure of how strongly the magnetization of a magnetic layer is aligned perpendicular to the film plane. A large value of the PMA is favored for realizing a small device size as well as a long data retention time. Indeed, the data retention time is governed by the thermal stability (Δ) as depicted by the relation $\Delta = k_{eff}V/k_BT$, where k_{eff} is the effective magnetic anisotropy, V is the volume of the device, k_{B} is the Boltzmann constant, and T is the temperature, respectively. Previous works have demonstrated that a large PMA can be obtained in 3*d*-ferromagnet (FM)/oxide magnetic stacks due to the polarization of the orbital magnetic moment to out-of-plane direction by oxygen hybridization between 3*d*-orbitals of the FM and a *p*-orbital of the oxide[22-24].The Gilbert damping (α) is a measure of the energy dissipation during the magnetization transition, which is preferred to be small as possible for efficient spin manipulation as it appears that the critical current density for the magnetization switching by the STT and the SOT is commonly proportional to α (Ref. [13, 25]). Additionally, small α is helpful to decrease the write-error rate (WER) when the magnetization switching is operated by the VCMA[26]. So far, many efforts to achieve the ultra-low Gilbert damping have been carried out throughout optimizing the composition ratio in binary magnetic alloys and/or by designing an stack which minimizes adverse effects, such as spin pumping[27-32].

In modern spintronics, the magnetic tunnel junction (MTJ) with an MgO insulation layer sandwiched by two FM layers (e.g. Fe/MgO/Fe) is the most popular device type since then a large tunnel magnetoresistance (TMR) is reported in this structure[33, 34]. Furthermore, CoFeB/MgO/CoFeB stacks sandwiched by two Ta layers, i.e. Ta/CoFeB/MgO/CoFeB/Ta, is the most conventional structure for MTJs aiming for a large PMA[21]. The presence of the Ta layers, however, inevitably contributes to an increase of α due to a large spin-to-charge conversion in the Ta layer arising from the spin pumping[16, 35]. Towards the concurrent achievement of ultra-low α and large PMA, alternative structures replacing the Ta layers to oxide (e.g. MgO) layers have been considered (double-barrier structures). Regrettably, an additional substitution into the FM layers, i.e. a multi-layered FM e.g. CoFeB/X/CoFeB (X= a metal such as Ta, Ir, W, or Mo) replacing the single-layered CoFeB layer, is necessary to prevent the degradation of crystallinity and maintain the PMA, where the material X layer acts as a B-atoms absorber[36-43]. Considering that multi-layered FM layers are far from optimized, particularly in terms

of the difficulty in achieving a small α (Ref. [44]), further consideration is strongly requested.

Here we investigate the magnetic properties in CoFeB-based double-barrier magnetic stacks with a GdOx inserted capping layer. So far, there have been several reports on the VCMA in magnetic stacks containing GdOx, focusing on its high oxygen ion mobility[45-47]. Additional work focused the role of GdOx as a B atoms absorber in order to improve the crystallinity of the FM layers[48]. Instead, we pay attention to another unique property of GdOx: that it strongly tends to combine with oxygen atoms due to a significantly large magnitude of enthalpy (~-1820 kJ/mol)[49]. This property enhances structural stability during the annealing process by suppressing the unintended diffusion of composite elements inside the stacks. Additionally, it opens another opportunity to vary the magnetic properties by altering the oxygen doping rate of the GdOx layer. In this work, we find that the GdOx insertion plays a substantial role in the enhancement of the PMA and the suppression of the Gilbert damping.

Sample preparation

We prepare $Mg_{40}Fe_{10}O_{50}$ (2.0)/$Co_{40}Fe_{40}B_{20}$ (t_{CFB})/GdOx (t_{GdOx})/MgO (0.95) (w/ GdOx) stacks sandwiched between a Si-SiOx substrate/Ta/TaB underlayer and a Ru/Ta/Ru capping layer (left panel of Fig. 1(a), numbers in parenthesis are in nm). Also, we prepare $Mg_{40}Fe_{10}O_{50}$ (2.0)/$Co_{40}Fe_{40}B_{20}$ (t_{CFB})/MgO (0.95) (w/o GdOx) stacks, in which the GdOx insertion layer is excluded, as control samples (Right panel of Fig. 1(a)). For simplicity, we denote $Mg_{40}Fe_{10}O_{50}$ and $Co_{40}Fe_{40}B_{20}$ as MgFeO and CoFeB, respectively. The ranges of t_{CFB} and t_{GdOx} are 1.0 nm$\leq t_{CFB} \leq$ 1.5 nm, and 0.2 nm$\leq t_{GdOx} \leq$1.2 nm, respectively. We would like to note that the adoption of MgFeO as an underlayer rather than MgO provides better wettability for the CoFeB layer, likely coming from the segregation of Fe^{2+} in the MgFeO layer[42, 50, 51]. All the stacks are prepared with an ultrahigh-vacuum magnetron sputtering chamber system (EXIM) manufactured by Tokyo Electron Ltd. The deposition of the CoFeB layer is carried out at low temperature (100 K) that contributes to an improvement of the MgFeO/CoFeB interface quality[43, 52]. The GdOx insertion layer is prepared by the successive Gd deposition and the natural oxidation equipped in the sputtering chamber. We varied the degree of the oxidation of the GdOx insertion layer which is quantified by the effective doping rate D_{eff} (See Supplementary material S1 for details on the preparation of the GdOx layer). After the deposition, all the stacks are post-annealed in the range of 250-400 °C in vacuum without the application of magnetic field.

Results and discussion

A static observation of magnetic properties was deduced by the vibrating sample magnetometer (VSM) measurement to obtain the saturation magnetization (M_s) and the effective magnetic anisotropy (k_{eff}). Here, we conduct the VSM measurement by applying magnetic field along the *z*-axis and in-plane axis (right panel in Fig. 1(a)). k_{eff} is evaluated by calculating the change in the area of a magnetization-magnetic field curve (*M-H* curve) depending on the magnetic field direction (along *z*-axis or in-plane axis)[53]. In this paper, k_{eff} is defined positive when the easy axis is along the *z*-axis, whereas it is negative when the easy axis is along the in-plane axis.

We first carry out the VSM measurement on magnetic stacks with fixed t_{CoFeB}=1 nm. Figure 1(b) presents magnetic curves under the magnetic field (H) application along the z-axis for a w/ GdOx [t_{GdOx}=0.2 nm and D_{eff}=150 sccm] and a w/o GdOx stack. As shown in upper panel, the magnetization of both the stacks favors to align along the z-axis after 250 °C annealing (T_A=250 °C). However, the easy axis remains the z-axis only for the w/ GdOx stack and moves to the in-plane axis for the w/o GdOx stack after 400 °C annealing (T_A=400 °C, bottom panel). The effective PMA energy density ($k_{eff}t_{CFB}$) designated by product of k_{eff} and t_{CFB} as a function of T_A is displayed in Fig. 1(c). Remarkably, $k_{eff}t_{CFB}$ for the w/ GdOx stacks maintains positive, while that for the w/o GdOx stacks shift to ~0 or to a negative value after the annealing at high temperature ($T_A \geq 350$ °C). This distinct behavior implies that the insertion of the GdOx layer plays some substantial role inside the stacks. Next, we investigate the $k_{eff}t_{CFB}$ dependency on T_A, t_{GdOx} and D_{eff} to clarify the influence of the GdOx insertion layer fixing t_{CFB}=1 nm. Figure 2 (a) displays $k_{eff}t_{CFB}$ as a function of T_A for the w/ GdOx stacks with various GdOx thicknesses. Note that D_{eff} is fixed to 150 sccm here. We find a huge variation of $k_{eff}t_{CFB}$ which ranges from >0.4 erg·cm^{-2} [t_{GdOx}=0.2 nm with T_A=250 or 300 °C] to ~0 erg·cm^{-2} [t_{GdOx}=1.2 nm with T_A=400 °C] depending on t_{GdOx} and T_A. Except for the stacks with t_{GdOx} =1.2 nm, the easy axis remains along the z-axis even though T_A is sufficiently high in the w/ GdOx stacks, contrasting to the behavior of the w/o GdOx stacks (Fig. 1(c)). Notably, stacks with a thinner GdOx layer have relatively larger $k_{eff}t_{CFB}$ values in general. Figure 2(b) displays $k_{eff}t_{CFB}$ in stacks with various D_{eff} in the range of 9 sccm ≤ D_{eff} ≤ 300 sccm. $k_{eff}t_{CFB}$ for the stacks with D_{eff}=9 sccm monotonically decreases as a function of T_A with a drastic change ranged from ~0.6 erg·cm^{-2} to < 0.1 erg·cm^{-2}. We would like to note that $k_{eff}t_{CFB}$ remains positive in the studied range of T_A different to the behavior of $k_{eff}t_{CFB}$ for the w/o GdOx stack (Fig. 1(c)), even though infinitesimal oxygen is doped in the GdOx insertion layer. On the contrary, the variation in $k_{eff}t_{CFB}$ for the stacks with D_{eff}=300 sccm is much suppressed, having maximum $k_{eff}t_{CFB}$ in the stack with T_A =300 °C rather than the stack with T_A=250 °C. The tendency of the stacks with D_{eff}=150 sccm is similar to that of the stacks with D_{eff}=300 sccm, but $k_{eff}t_{CFB}$ is much larger regardless of T_A. Except T_A =250 °C, $k_{eff}t_{CFB}$ is the largest in the stacks with D_{eff}=150 sccm at each T_A. We suppose that the D_{eff} dependence in Fig. 2(b) might be associated with a variation of orbital hybridization among the Fe-3d orbitals and O-2p orbital as a function of the oxygen concentration at the interfaces[22, 23, 54].

To clarify the role of the GdOx insertion layer more clearly, we carry out the cross-sectional bright-field (BF-) scanning transmission electron microscope (STEM), the nano-beam electron diffraction (NBED) and the energy dispersive X-ray spectroscopy (EDS) observations for the w/o GdOx (Fig. 3(a), (d), (g), (h)), the w/ GdOx with t_{GdOx} =0.6 nm (Fig. 3(b), (e), (i)) and the w/ GdOx with t_{GdOx} =1.2 nm (Fig. 3(c), (f), (j)) stacks. Note that all the observed stacks are fixed to t_{CFB} =1.0 nm and annealed at 350 °C, and all the w/ GdOx stacks are doped with D_{eff}=150 sccm. The 30-nm-thick TEM lamellae were prepared by a thickness-controllable script using FIB-SEM dual-beam Helios5UX with AutoScript program (Thermo Fisher Scientific) while considering FIB-damage becomes minimized[55, 56]. The STEM investigation was carried out at 300 kV accelerating voltage with convergence angle of 30 mrad using Spectra Ultra S/TEM (Thermo Fisher Scientific). Regardless of

the stacks, B atoms appear diffused from the CoFeB layer to both the upper and bottom layers in all the stacks as shown in the EDS observations (Fig. 3(d)-(j)). In other words, we do not find a clear GdOx insertion influence on the B atom diffusion. On the other hand, we find an obvious difference in the quality of the CoFeB layer. Both the STEM images and the NBED patterns indicate that the crystallinity of the CoFeB layer is improved in order of the w/o GdOx, the w/ GdOx [t_{GdOx} =0.6 nm], and the w/ GdOx [t_{GdOx} =1.2 nm] stack. For the w/o GdOx stack, we find intermixed regions among the MgFeO, CoFeB, and MgO layer as represented by cut-off regions in the CoFeB layer shown in the STEM image and the EDS elemental map for Fe (Fig. 3(a), (d)). Also, a mixed region among Co, Fe, Mg and O elements appears in the EDS line profiles for the w/o GdOx stacks which is particularly apparent along the path (2), strongly supporting the active intermixing we observe (Fig. 3(g), (h)). We suppose that such drastic decrease of $k_{eff}t_{CFB}$ in the high T_A regime for the w/o GdOx stacks comes from a significant intermixing which destroys the optimal orbital hybridization at both the MgFeO/CoFeB and the CoFeB/MgO interfaces. In this respect, we also speculate that the intermixing might be moderate when T_A is low ($T_A \leq 300$ °C), owing to the considerable $k_{eff}t_{CFB}$ (Fig. 1(c)). On the contrary, clear segregations among the layers are shown in the w/ GdO stacks (Fig. 3(b)-(c), (e)-(f), (i)-(j)). The suppression of the intermixing in the w/ GdOx stacks offers better crystallinity of the CoFeB layers as supported by the NBED patterns (Fig. 3(a)-(c)). The remarkable intermixing for the w/o GdOx stack is understandable considering that Fe atoms and O atoms prefers to combine each other since the magnitude of enthalpy for MgO (~-601.6 kJ/mol) is much smaller than that for FeOx (Fe_2O_3:~-824.2 kJ/mol and Fe_3O_4:~-1118.4 kJ/mol). This active intermixing is relieved when inserting the GdOx layer due to its huge magnitude of enthalpy (~-1820 kJ/mol). Meanwhile, we find relatively less differences between the two w/ GdOx stacks in the STEM images and the EDS line profiles. Particularly, we commonly find an intermixing between the MgO and the GdOx layer in both the stacks. However, still there are some differences between the two stacks as followings: (I) Different features on Gd peaks at the MgO+GdOx/CoFe interface where the Gd peak in the stack with t_{GdOx}=0.6 nm is broader and significantly overlapped with the Co and Fe peaks contrasting to a separated and sharp peak for the that with t_{GdOx}=1.2 nm (Fig. 3(i), (j)). (II) A better crystallinity of the CoFeB layer in the stack with t_{GdOx} =1.2 nm as supported by the NBED patterns (Fig. 3(b), (c), (Also find Supplementary material S2 for details on the NBED)). We speculate that the suppressed diffusion of Gd atoms as supported by (I) might be a reason why the better crystallinity is shown the stack with t_{GdOx} =1.2 nm (II). Furthermore, the different crystallinity inevitably brings about changes in the band structures, which potentially alter the orbital hybridization among the Fe-3*d* orbitals and the O-2*p* orbital[23, 57, 58]. Indeed, a previous work pointed out a possibility that a change in crystallinity could alter orbital hybridization[59].

Next, we attempted to verify how much we can expand the range of t_{CFB} in stacks that exhibit a positive k_{eff}. Conventionally, a thick FM layer is known to be beneficial in terms of realizing small α (ref. [31, 60]). Before the verification, we observe $k_{eff}t_{CFB}$ for the w/o GdOx stacks in the range of 1.0 nm $\leq t_{CFB} \leq$ 1.5 nm (Fig. 4(a)). Similar to the tendency shown in Fig. 1(c), $k_{eff}t_{CFB}$ abruptly drops as T_A

becomes larger than 350 °C for all the stacks. Furthermore, $k_{eff}t_{CFB}$ decreases significantly with increase of t_{CFB} even though T_A=250 °C, and no longer $k_{eff}t_{CFB}$ has remained positive when t_{CFB} > 1.4 nm. The decrease of $k_{eff}t_{CFB}$ with the increase of t_{CFB} is understandable considering that the bulk component, e.g. the demagnetization field, is proportional to t_{CFB}, providing an adverse effect for $k_{eff}t_{CFB}$ (Ref. [53, 61]). We compare $k_{eff}t_{CFB}$ values from w/ GdOx stacks with t_{CFB}=1.0, 1.1 and 1.2 nm. The values of t_{GdOx} and D_{eff} are fixed to 0.2 nm and 150 sccm (300 sccm), respectively, in Fig. 4(b) (Fig. 4(c)). When D_{eff}=150 sccm, all the stacks are showing $k_{eff}t_{CFB}$> 0, while the stacks with t_{CFB}=1.0 nm have the largest values of $k_{eff}t_{CFB}$ regardless of T_A. The tendency alters significantly when D_{eff}=300 sccm, the stacks with t_{CFB}=1.0 nm have the smallest values of $k_{eff}t_{CFB}$ regardless of T_A although all the stacks still show positive $k_{eff}t_{CFB}$. Remarkably, both the stacks with t_{CFB}=1.1 and 1.2 nm reach a maximum ~0.5 erg·cm^{-2} of $k_{eff}t_{CFB}$. This implies that a large value of t_{CFB} no longer corresponds to a small value of $k_{eff}t_{CFB}$, in stark contrast to the behavior of $k_{eff}t_{CFB}$ for the w/o GdOx stacks (Fig. 4(a)). Figure 4(d) presents $k_{eff}t_{CFB}$ as a function of D_{eff} for several annealing temperatures when t_{CFB} is fixed to 1.2 nm. Except for the stacks with T_A=250 °C, $k_{eff}t_{CFB}$ reaches maximum when the GdOx layers are doped with D_{eff}=500 or 700 sccm. It is contrasting to the results for t_{CFB}=1.0 nm where D_{eff} =150 sccm is required for the optimal $k_{eff}t_{CFB}$ value except T_A=250 °C (Fig. 2(b)). Remarkably, the maximum $k_{eff}t_{CFB}$ value is more than 0.5 erg·cm^{-2} which is slightly larger than the maximum $k_{eff}t_{CFB}$ observed in the stacks with t_{CFB}=1.0 nm. Next, we attempt to observe $k_{eff}t_{CFB}$ for stacks with t_{CFB} =1.4 nm and 1.5 nm (Fig. 4(e)). The observed maximum $k_{eff}t_{CFB}$ is still considerable as ~0.4 erg·cm^{-2} among the stacks with t_{CFB}=1.4 nm. Also, we find $k_{eff}t_{CFB}$ reaches the maximum ~0.3 erg·cm^{-2} in the range of our investigation when t_{CFB}=1.5 nm. Overall, it appears that a higher D_{eff} is favored to get a large $k_{eff}t_{CFB}$ when increasing t_{CFB}. In other words, a greater amount of oxygen should be supplied to obtain an optimal interfacial state for large $k_{eff}t_{CFB}$ (Find Supplementary material S3 for full data set of $k_{eff}t_{CFB}$). A previous literature pointed out that the local chemical bonding between Fe and O atoms is significantly influenced by the thickness and the crystallinity of a ferromagnet layer[59]. We presume that the different bonding near the interface alters the optimal stoichiometry of oxygen atoms.

Additional to the static observation by the VSM, we also carry out a dynamic observations via the ferromagnetic resonance (FMR) measurement[62]. The FMR measurement is performed under the application of a magnetic field along the z-axis (Fig. 1(a)). A typical FMR spectrum, derivative of magnetic susceptibility ($\partial\chi/\partial H$) as a function of H, is exhibited in Fig. 5(a). Here, the resonance field (H_R) depends on the frequency (f) of the applied radiofrequency field governed by the Kittel formula:

$$f = \frac{\gamma}{2\pi}\left(H_R - 4\pi M_{eff}\right) \quad (1)$$

where γ is the gyromagnetic ratio and M_{eff} is the effective magnetization, respectively[63]. Here, $\gamma = g^{\perp}\mu_B/\hbar$, where $g^{\perp}$ is the perpendicular component of the Lande g-factor, μ_B is the Bohr magneton, and $\hbar$ is the reduced Planck constant, respectively. And $4\pi M_{eff} = 4\pi M_s - H_k$, where H_k is the anisotropy field. Figure 5(b) displays H_R as a function of f for stacks with $k_{eff}t_{CFB} > 0$ and $k_{eff}t_{CFB} < 0$. The slopes of the fittings are somewhat unlike each other, indicating different values of $g^{\perp}$ as $g^{\perp}$= 2.13

and 2.04 for the former and the latter cases, respectively.

The Gilbert damping α is deduced by the analysis of the FMR spectrum, where the half-linewidth is associated with α by a following relation[64]:

$$\Delta H = \frac{2\pi\alpha\hbar}{g^{\perp}\mu_B} f + \Delta H(0) \quad (2)$$

where ΔH and $\Delta H(0)$ are the half-linewidth at finite f and 0 Hz, respectively. ΔH as a function of f for the w/o GdOx and the w/ GdOx stacks exhibited in Fig. 5(c). t_{CFB} of the w/o GdOx stack is 1.0 nm, and that of the w/ GdOx stack changes from 1.0 nm to 1.4 nm, while fixing t_{GdOx}=0.2 nm. Data for the w/ GdOx stacks in Fig. 5(c), indeed, are collected from stacks with the smallest or mostly close to the smallest values of α in each t_{CFB}. We note that all the data presented in Fig. 5(c) are obtained from stacks with T_A=350 °C. Overall, the slope for the w/ GdOx stacks is considerably smaller than that for the w/o GdOx stack. Evaluated α for the w/o GdOx stack is 3.86×10^{-3}. Regarding on the w/ GdOx stacks, the slope decreases with increase of t_{CFB}, indicating α varies 2.63×10^{-3}, 2.26×10^{-3}, 1.68×10^{-3} for the stacks with 1.0, 1.2, and 1.4 nm of t_{CFB}, respectively. Here we would like to note that all the w/GdOx stacks presented in Fig. 5(c) have positive $k_{eff}t_{CFB}$ values. The evaluated α values are close to the smallest values reported in literatures up to date: 2.63×10^{-3} of α for the w/GdOx stack with t_{CFB}=1.0 nm in this study is similar with the smallest α among series of CoFe/Ta stacks with 10 nm of the CoFe thickness in Ref. [28]. Moreover, 1.68×10^{-3} of α for the w/GdOx stack with t_{CFB}=1.4 nm in this study is comparable to that for an epitaxially grown MgAlO/CoFe/Cr stack with 6.8 nm of the CoFe thickness ($\alpha < 1.21\times10^{-3}$) in Ref. [29]. We note that all the stacks in the previous studies have negative $k_{eff}t_{CFB}$, contrasting to the w/GdOx stacks in Fig. 5(c). All the observed values of α in this investigation are exhibited in Fig. 5(d). We find that α becomes small considerably as $t_{CFB} > 1.0$ nm. Particularly, a great increase of α in T_A=400 °C is shown in the stacks with t_{CFB}=1.0 nm but disappears in all the stacks with $t_{CFB} > 1.0$ nm. If a condition with $t_{CFB} > 1.0$ nm and $T_A > 250$ °C holds, it appears that α mostly depends on D_{eff} rather than other factors. Remarkably, we find numbers of points with $\alpha < 2.00\times10^{-3}$, and the smallest observed value of α is 1.68×10^{-3}. The data shown in Fig. 5(d) strongly supports that efforts to broadening the range of t_{CFB} in stacks that having $k_{eff}t_{CFB} > 0$ is worthy, in terms of the concurrent achievement of large PMA and ultra-low damping.

In general, α consists of intrinsic and extrinsic component as below:

$$\alpha = \alpha_{int} + \alpha_{ext} = \alpha_{int} + \alpha_{sp} + \alpha_{TMS} + \alpha_{rad} \quad (3)$$

where α_{int} and α_{ext} are the intrinsic and the extrinsic component of the damping, respectively. And α_{sp}, α_{TMS}, and α_{rad} are the damping caused by the spin-pumping[35], the two-magnon scattering[65], and the radiofrequency coupling[66], respectively. Although there are many components that could act on α_{ext} in principle, their contribution would be trivial for all the investigated stacks in this work. A considerable α_{sp} value would require a large spin-to-charge conversion conduction material, such as Ta or Pt, neighbored to a magnetic layer[27, 67]. Thanks to that we adopt the double-barrier structure in which a FM layer is sandwiched by oxide insulators, α_{sp} should be negligible[27, 31]. The values of α_{TMS}, and α_{rad} are also trivial considering our measurement configuration under the application of a magnetic field

along the z-axis as well as the ultrathin thicknesses of the CoFeB layers used in all the investigated stacks[28, 66]. The minimization of α_{ext} is therefore attributed to be the main reason why we obtain such a small α in the GdOx inserted stacks. Meanwhile, we consider that α_{int} would also vary depending on lots of parameters, such as T_A, t_{CFB}, and D_{eff}, which are controlled during the sample preparation. The variations of those conditions could alter the internal energy state, and subsequently the density of states. Indeed, the density of states near the Fermi level is directly associated with α_{int} (Ref. [28, 68, 69]). In this respect, there is a possible adverse effect on α_{int} by the interfacial PMA, considering that the PMA would generate a non-uniform effective magnetic field inside a stack[70]. This might be one reason why a stack with the largest $k_{eff}t_{CFB}$ is not identical to a stack with the smallest α amongst the same t_{CFB} stacks. Nevertheless, α_{int} maintains a small value in all the investigated stacks due to the adoption of the single-layered FM layer[44] and the cryogenic deposition[71]. Moreover, the GdOx insertion may contribute to the suppression of α_{int}, preventing the unintended intermixing among the layers and allowing a crystallinity improvement of the CoFeB layer during the annealing process (Fig. 2). This is a reason why the w/ GdOx stacks generally have smaller α values than the w/o GdOx stacks[31]. Also, the increase of t_{CFB} may assist in decreasing adverse effects from the interfaces, albeit a relation between α_{int} and t_{CFB} is not defined quantitatively different to the case of α_{ext} (Ref. [31, 60]).

Finally, we consider the relation between k_{eff} and $g^{\perp}$. Surprisingly, all the results tend to collapse to one curve (Fig. 6). Indeed, $g^{\perp}$ follows a following relation,

$$g^{\perp} = 2 + \frac{m_L^{\perp}}{m_s} \quad (4)$$

where $m_L^{\perp}$ and m_s are the perpendicular component of the orbital magnetic moment and the spin magnetic moment, respectively[63, 72]. According to previous studies, m_s is relatively insensitive to the layer thickness or the annealing temperature[63, 73, 74]. In that sense, it is likely that the variation of $g^{\perp}$ may mainly reflect the change in $m_L^{\perp}$. Hence, we suppose that the relation between k_{eff} and $g^{\perp}$ shown in Fig. 6 implies that the PMA in all the observed stacks is dominantly governed by the polarization of the orbital magnetic moment. This implies that all the changes in conditions during the sample preparation, indeed, may contribute to varying the polarization of the orbital magnetic moment. Particularly, a virtue of the GdOx insertion is that $m_L^{\perp}$ maintains large even in stacks with large t_{CFB} throughout the modulation of the conditions such as D_{eff}. Remarkably, this assists the concurrent achievement of large PMA and ultra-low Gilbert damping.

Conclusions

In this work, we have demonstrated the concurrent achievement of a large PMA value and ultra-low Gilbert damping in the GdOx inserted double-barrier MgFeO/CoFeB/GdOx/MgO stacks. The insertion of the GdOx as a capping layer prevents the unintended intermixing among the CoFeB layer and the oxide layers due to GdOx's large magnitude of enthalpy, as supported by the material characterization. Also, it broadens the range of the FM thickness in stacks that satisfies considerable PMA, while suppressing the Gilbert damping at an ultra-low level. A consideration of the Lande *g*-factor informs

us that the magnitude of the effective PMA in the investigated stacks is deeply associated with the polarization of the orbital magnetic moment. The polarization of the orbital magnetic moment can be controlled by the modulation of conditions such as the oxygen doping rate of the GdOx layer. Hence, we believe that the modulation of oxygen doping rate might be a useful tool for the material designing of spintronic devices hereafter.

The authors acknowledge the assistance of T. Scheike, K. Ohba, and M. Hosomi in fruitful discussions. We appreciate the financial support from New Energy and Industrial Technology Development Organization (NEDO) project (Grants No. JPNP 16007). J. K. appreciates the financial support from Japan Society for the Promotion of Science (JSPS) KAKENHI (Grants No. JP23K04574). A part of this work was supported by the Electron Microscopy Unit, National Institute for Materials Science (NIMS).

1. C. Chappert, A. Fert and F. N. Van Dau, Nat Mater **6** (11), 813-823 (2007).

2. K. Ando, S. Fujita, J. Ito, S. Yuasa, Y. Suzuki, Y. Nakatani, T. Miyazaki and H. Yoda, J Appl Phys **115** (17), 172607 (2014).

3. J. Grollier, D. Querlioz, K. Y. Camsari, K. Everschor-Sitte, S. Fukami and M. D. Stiles, Nature Electronics (2020).

4. J. Torrejon, M. Riou, F. A. Araujo, S. Tsunegi, G. Khalsa, D. Querlioz, P. Bortolotti, V. Cros, K. Yakushiji, A. Fukushima, H. Kubota, S. Yuasa, M. D. Stiles and J. Grollier, Nature **547**, 428 (2017).

5. W. A. Borders, A. Z. Pervaiz, S. Fukami, K. Y. Camsari, H. Ohno and S. Datta, Nature **573** (7774), 390-393 (2019).

6. M. Weisheit, S. Fähler, A. Marty, Y. Souche, C. Poinsignon and D. Givord, Science **315** (5810), 349-351 (2007).

7. MaruyamaT, ShiotaY, NozakiT, OhtaK, TodaN, MizuguchiM, A. A. Tulapurkar, ShinjoT, ShiraishiM, MizukamiS, AndoY and SuzukiY, Nat Nano **4** (3), 158-161 (2009).

8. Y. Shiota, T. Nozaki, F. Bonell, S. Murakami, T. Shinjo and Y. Suzuki, Nat Mater **11** (1), 39-43 (2012).

9. T. Nozaki, T. Yamamoto, S. Miwa, M. Tsujikawa, M. Shirai, S. Yuasa and Y. Suzuki, Micromachines **10** (5), 327 (2019).

10. T. Yamamoto, R. Matsumoto, T. Nozaki, H. Imamura and S. Yuasa, J Magn Magn Mater **560**, 169637 (2022).

11. J. C. Slonczewski, J Magn Magn Mater **159** (1–2), L1-L7 (1996).

12. L. Berger, Phys Rev B **54** (13), 9353-9358 (1996).

13. D. C. Ralph and M. D. Stiles, J Magn Magn Mater **320** (7), 1190-1216 (2008).

14. S. I. Kiselev, J. C. Sankey, I. N. Krivorotov, N. C. Emley, R. J. Schoelkopf, R. A. Buhrman and D. C. Ralph, Nature **425** (6956), 380-383 (2003).

15. I. M. Miron, K. Garello, G. Gaudin, P.-J. Zermatten, M. V. Costache, S. Auffret, S. Bandiera, B. Rodmacq, A. Schuhl and P. Gambardella, Nature **476**, 189-193 (2011).

16. L. Liu, C.-F. Pai, Y. Li, H. W. Tseng, D. C. Ralph and R. A. Buhrman, Science **336** (6081), 555-558 (2012).

17. J. Sinova, S. O. Valenzuela, J. Wunderlich, C. H. Back and T. Jungwirth, Reviews of Modern Physics **87** (4), 1213-1260 (2015).

18. J. Kim, D. Go, H. Tsai, D. Jo, K. Kondou, H.-W. Lee and Y. Otani, Phys Rev B **103** (2), L020407 (2021).

19. J. Kim and Y. Otani, J Magn Magn Mater **563**, 169974 (2022).

20. S. Lee, M.-G. Kang, D. Go, D. Kim, J.-H. Kang, T. Lee, G.-H. Lee, J. Kang, N. J. Lee, Y. Mokrousov, S. Kim, K.-J. Kim, K.-J. Lee and B.-G. Park, Communications Physics **4** (1), 234 (2021).

21. S. Ikeda, K. Miura, H. Yamamoto, K. Mizunuma, H. D. Gan, M. Endo, S. Kanai, J. Hayakawa, F. Matsukura and H. Ohno, Nat Mater **9** (9), 721-724 (2010).

22. B. Rodmacq, A. Manchon, C. Ducruet, S. Auffret and B. Dieny, Phys Rev B **79** (2), 024423 (2009).

23. H. X. Yang, M. Chshiev, B. Dieny, J. H. Lee, A. Manchon and K. H. Shin, Phys Rev B **84** (5), 054401

(2011).
24. J. W. Koo, S. Mitani, T. T. Sasaki, H. Sukegawa, Z. C. Wen, T. Ohkubo, T. Niizeki, K. Inomata and K. Hono, Appl Phys Lett **103** (19), - (2013).
25. FukamiS, AnekawaT, ZhangC and OhnoH, Nat Nano **11**, 621-625 (2016).
26. Y. Shiota, T. Nozaki, S. Tamaru, K. Yakushiji, H. Kubota, A. Fukushima, S. Yuasa and Y. Suzuki, Appl Phys Express **9** (1), 013001 (2016).
27. M. Konoto, H. Imamura, T. Taniguchi, K. Yakushiji, H. Kubota, A. Fukushima, K. Ando and S. Yuasa, Appl Phys Express **6** (Copyright (c) 2013 The Japan Society of Applied Physics), 073002 (2013).
28. M. A. W. Schoen, D. Thonig, M. L. Schneider, T. J. Silva, H. T. Nembach, O. Eriksson, O. Karis and J. M. Shaw, Nat Phys **12**, 839 (2016).
29. A. J. Lee, J. T. Brangham, Y. Cheng, S. P. White, W. T. Ruane, B. D. Esser, D. W. McComb, P. C. Hammel and F. Yang, Nature Communications **8** (1), 234 (2017).
30. J. M. Shaw, E. K. Delczeg-Czirjak, E. R. J. Edwards, Y. Kvashnin, D. Thonig, M. A. W. Schoen, M. Pufall, M. L. Schneider, T. J. Silva, O. Karis, K. P. Rice, O. Eriksson and H. T. Nembach, Phys Rev B **97** (9), 094420 (2018).
31. E. R. J. Edwards, H. T. Nembach and J. M. Shaw, Physical Review Applied **11** (5), 054036 (2019).
32. M. Arora, E. K. Delczeg-Czirjak, G. Riley, T. J. Silva, H. T. Nembach, O. Eriksson and J. M. Shaw, Physical Review Applied **15** (5), 054031 (2021).
33. S. Yuasa, T. Nagahama, A. Fukushima, Y. Suzuki and K. Ando, Nat Mater **3** (12), 868-871 (2004).
34. S. S. P. Parkin, C. Kaiser, A. Panchula, P. M. Rice, B. Hughes, M. Samant and S.-H. Yang, Nat Mater **3** (12), 862-867 (2004).
35. Y. Tserkovnyak, A. Brataas and G. E. W. Bauer, Physical Review Letters **88** (11), 117601 (2002).
36. H. Sato, M. Yamanouchi, S. Ikeda, S. Fukami, F. Matsukura and H. Ohno, Appl Phys Lett **101** (2) (2012).
37. S. Couet, T. Devolder, J. Swerts, S. Mertens, T. Lin, E. Liu, S. Van Elshocht and G. Sankar Kar, Appl Phys Lett **111** (15) (2017).
38. S. Srivastava, A. P. Chen, T. Dutta, R. Ramaswamy, J. Son, M. S. M. Saifullah, K. Yamane, K. Lee, K.-L. Teo, Y. P. Feng and H. Yang, Physical Review Applied **10** (2), 024031 (2018).
39. M. Wang, W. Cai, K. Cao, J. Zhou, J. Wrona, S. Peng, H. Yang, J. Wei, W. Kang, Y. Zhang, J. Langer, B. Ocker, A. Fert and W. Zhao, Nature Communications **9** (1), 671 (2018).
40. H. Cheng, J. Chen, S. Peng, B. Zhang, Z. Wang, D. Zhu, K. Shi, S. Eimer, X. Wang, Z. Guo, Y. Xu, D. Xiong, K. Cao and W. Zhao, Advanced Electronic Materials **6** (8), 2000271 (2020).
41. T. Yamamoto, T. Nozaki, K. Yakushiji, S. Tamaru, H. Kubota, A. Fukushima and S. Yuasa, Acta Mater **216**, 117097 (2021).
42. T. Yamamoto, T. Ichinose, J. Uzuhashi, T. Nozaki, T. Ohkubo, K. Yakushiji, S. Tamaru, H. Kubota and S. Yuasa, Acta Mater **267**, 119749 (2024).
43. T. Nozaki, T. Ichinose, T. Yamamoto, K. Yakushiji and S. Yuasa, APL Materials **12** (9) (2024).
44. R. Urban, G. Woltersdorf and B. Heinrich, Physical Review Letters **87** (21), 217204 (2001).

45. U. Bauer, L. Yao, A. J. Tan, P. Agrawal, S. Emori, H. L. Tuller, S. van Dijken and G. S. D. Beach, Nat Mater **advance online publication** (2014).
46. C. Bi, Y. Liu, T. Newhouse-Illige, M. Xu, M. Rosales, J. W. Freeland, O. Mryasov, S. Zhang, S. G. E. te Velthuis and W. G. Wang, Physical Review Letters **113** (26), 267202 (2014).
47. R. Mishra, F. Mahfouzi, D. Kumar, K. Cai, M. Chen, X. Qiu, N. Kioussis and H. Yang, Nature Communications **10** (1), 248 (2019).
48. D. W. Y. Lee, J. Li, T. Nagase, K. Sawada, T. Oikawa, K. Yoshino, T. Isoda, Japan Patent No. 特開 2019-165158 (2019).
49. J. A. Dean, (McGraw-Hill, New York, 1979).
50. K. Yakushiji, E. Kitagawa, T. Ochiai, H. Kubota, N. Shimomura, J. Ito, H. Yoda and S. Yuasa, AIP Advances **8** (5) (2017).
51. T. Ichinose, T. Yamamoto, T. Nozaki, K. Yakushiji, S. Tamaru and S. Yuasa, Appl Phys Express **16** (11), 113002 (2023).
52. T. Ichinose, T. Yamamoto, T. Nozaki, K. Yakushiji, S. Tamaru, M. Konoto and S. Yuasa, ACS Applied Electronic Materials **5** (4), 2178-2183 (2023).
53. J. Sinha, M. Hayashi, A. J. Kellock, S. Fukami, M. Yamanouchi, H. Sato, S. Ikeda, S. Mitani, S.-h. Yang, S. S. P. Parkin and H. Ohno, Appl Phys Lett **102** (24), 242405-242404 (2013).
54. A. Manchon, S. Pizzini, J. Vogel, V. Uhlir, L. Lombard, C. Ducruet, S. Auffret, B. Rodmacq, B. Dieny, M. Hochstrasser and G. Panaccione, J Appl Phys **103** (7), 07A912-913 (2008).
55. H. Tsurusawa, J. Uzuhashi, Y. Kozuka, K. Kimoto and T. Ohkubo, Small Methods **8** (9), 2301425 (2024).
56. J. Uzuhashi and T. Ohkubo, Ultramicroscopy **262**, 113980 (2024).
57. K. Nakamura, R. Shimabukuro, Y. Fujiwara, T. Akiyama, T. Ito and A. J. Freeman, Physical Review Letters **102** (18), 187201 (2009).
58. M. Tsujikawa and T. Oda, Physical Review Letters **102** (24), 247203 (2009).
59. Z.-P. Li, S. Li, Y. Zheng, J. Fang, L. Chen, L. Hong and H. Wang, Appl Phys Lett **109** (18), 182403 (2016).
60. L. Zhu, L. Zhu, D. C. Ralph and R. A. Buhrman, Physical Review Applied **13** (3), 034038 (2020).
61. T. Nozaki, A. Kozioł-Rachwał, M. Tsujikawa, Y. Shiota, X. Xu, T. Ohkubo, T. Tsukahara, S. Miwa, M. Suzuki, S. Tamaru, H. Kubota, A. Fukushima, K. Hono, M. Shirai, Y. Suzuki and S. Yuasa, NPG Asia Materials **9** (12), e451-e451 (2017).
62. S. Tamaru, S. Tsunegi, H. Kubota and S. Yuasa, Rev Sci Instrum **89** (5) (2018).
63. J. M. Shaw, H. T. Nembach and T. J. Silva, Phys Rev B **87** (5), 054416 (2013).
64. S. Karube, K. Kondou and Y. Otani, Appl Phys Express **9** (3), 033001 (2016).
65. R. Arias and D. L. Mills, Phys Rev B **60** (10), 7395-7409 (1999).
66. M. A. W. Schoen, J. M. Shaw, H. T. Nembach, M. Weiler and T. J. Silva, Phys Rev B **92** (18), 184417 (2015).
67. S. Ding, H. Wang, W. Legrand, P. Noël and P. Gambardella, Nano Letters (2024).
68. H. Ebert, S. Mankovsky, D. Ködderitzsch and P. J. Kelly, Physical Review Letters **107** (6), 066603

(2011).
69. S. Mankovsky, D. Ködderitzsch, G. Woltersdorf and H. Ebert, Phys Rev B **87** (1), 014430 (2013).
70. G. Woltersdorf, M. Kiessling, G. Meyer, J. U. Thiele and C. H. Back, Physical Review Letters **102** (25), 257602 (2009).
71. A. Sugihara, T. Ichinose, S. Tamaru, T. Yamamoto, M. Konoto, T. Nozaki and S. Yuasa, Appl Phys Express **16** (2), 023003 (2023).
72. H. Mizuno, T. Moriyama, K. Tanaka, M. Kawaguchi, T. Koyama, D. Chiba and T. Ono, Japanese Journal of Applied Physics **61** (10), 103001 (2022).
73. D. Weller, J. Stöhr, R. Nakajima, A. Carl, M. G. Samant, C. Chappert, R. Mégy, P. Beauvillain, P. Veillet and G. A. Held, Physical Review Letters **75** (20), 3752-3755 (1995).
74. J. Okabayashi, J. W. Koo, H. Sukegawa, S. Mitani, Y. Takagi and T. Yokoyama, Appl Phys Lett **105** (12), - (2014).

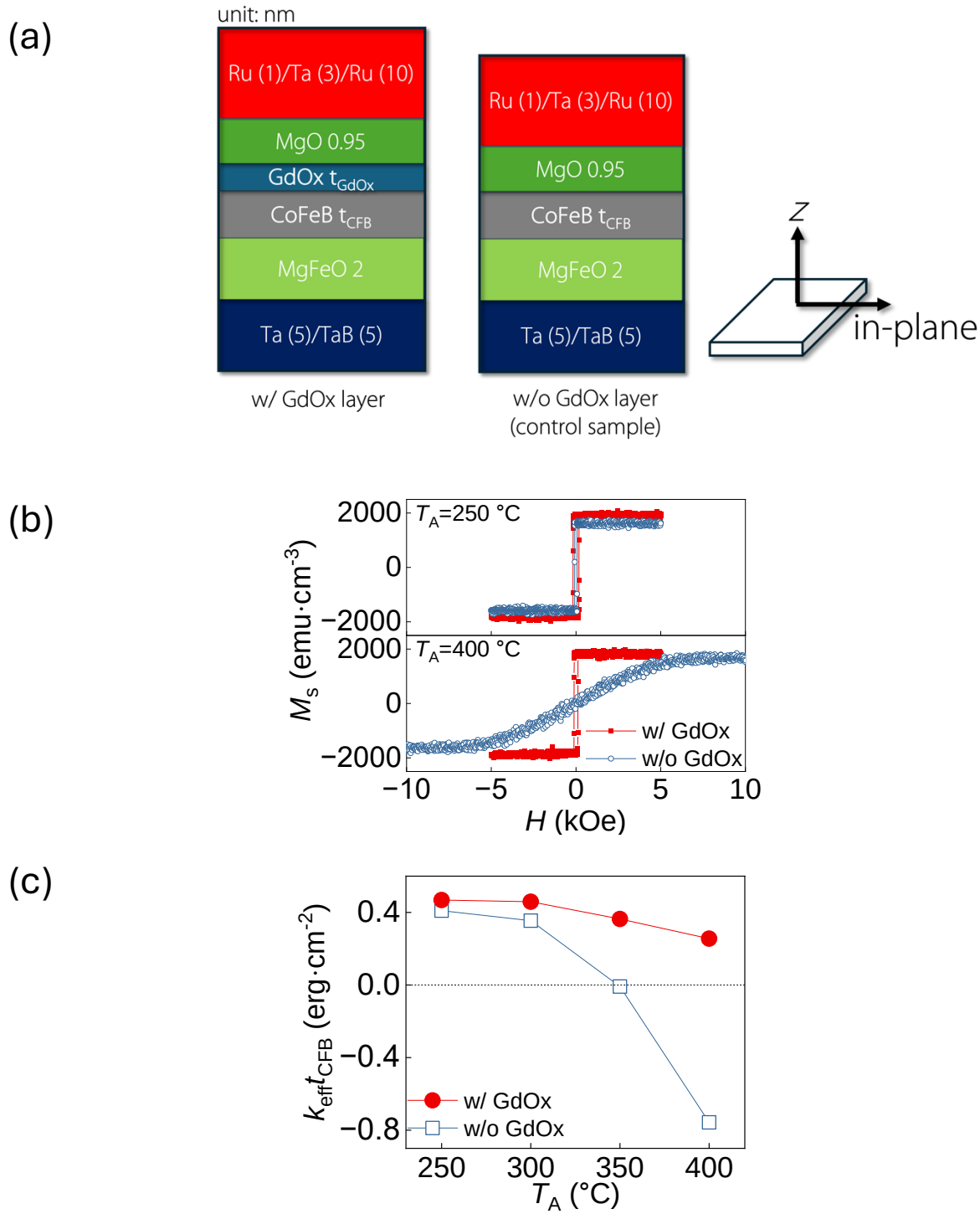

Fig. 1 (a) Layer structures of the w/ GdOx (left), and the w/o GdOx (middle) stack, respectively. Right panel presents the definition of axes in this investigation. (b) Hysteresis loops under the application of external field along to z-axis. Upper and bottom panel presents data for the stacks with T_A= 250 °C and 300 °C, respectively. (c) $k_{eff}t_{CFB}$ as a function of T_A. In both (b) and (c), red solid and blue open symbols for the w/ GdOx and the w/o GdOx stacks, respectively.

(a)

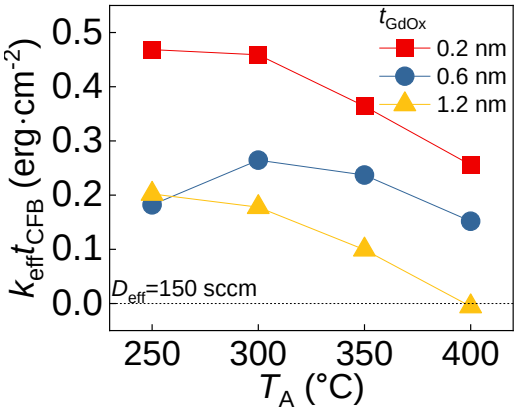

(b)

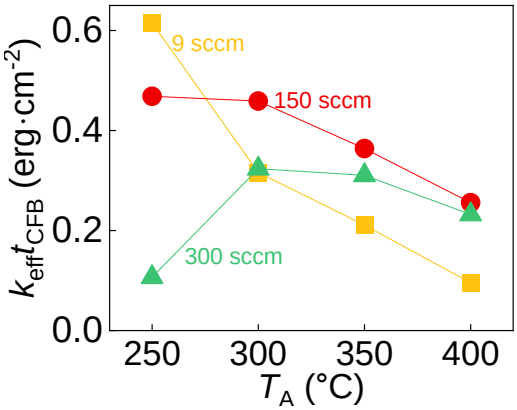

Fig. 2 (a) $k_{eff}t_{CFB}$ as a function of T_A for the stacks with 0.2 (red squares), 0.6 (blue circles), and 1.2 (yellow triangles) nm of t_{GdOx}. (b) $k_{eff}t_{CFB}$ as a function of T_A for the stacks with 9 (yellow squares), 150 (red circles), and 300 (green triangles) sccm of D_{eff}. Note that all the data are obtained from the stacks with $k_{eff}t_{CFB}$ = 1.0 nm.

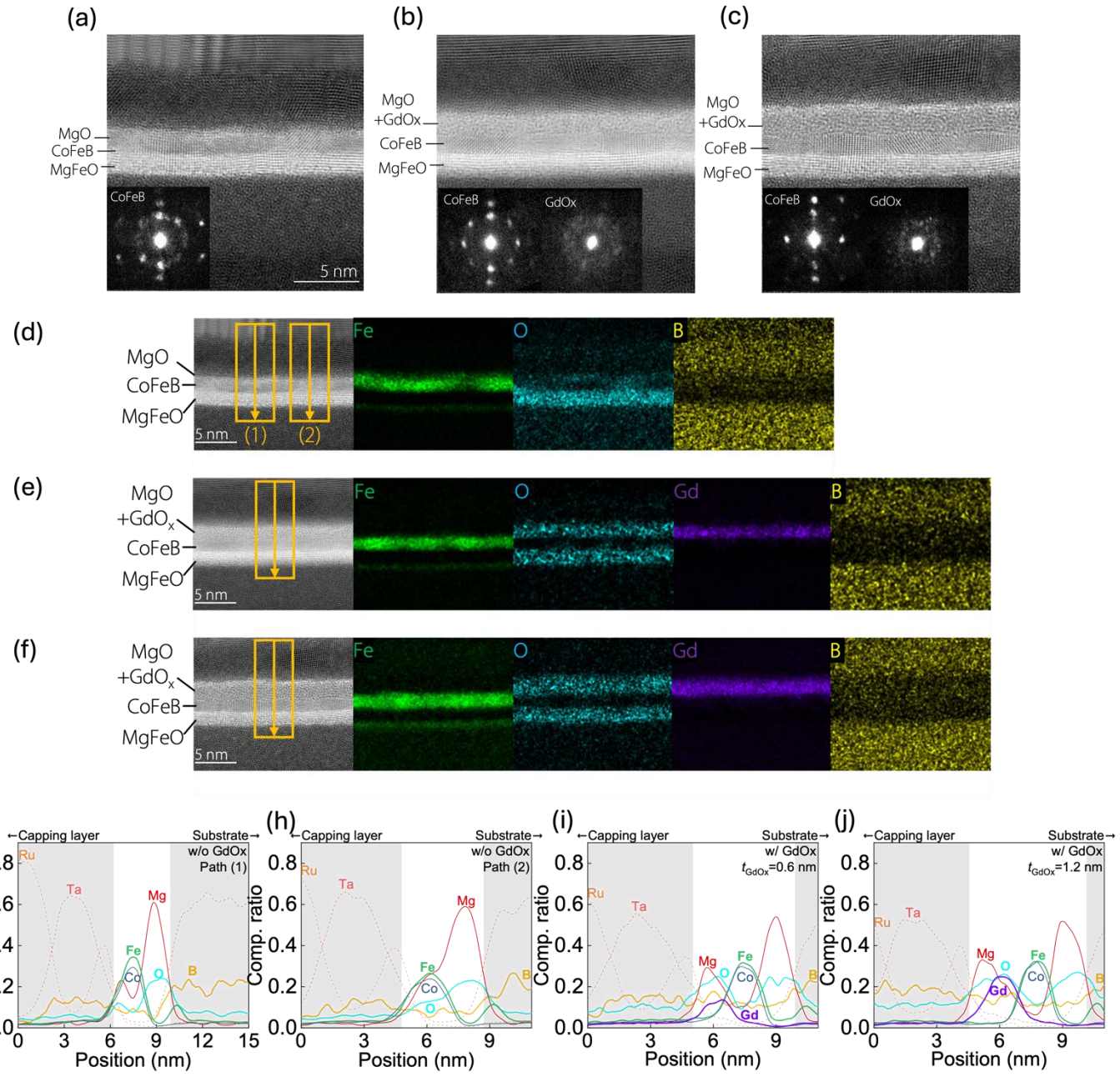

Fig. 3 (a), (b), (c) BF-STEM images and NBED patterns. (d), (e), (f) EDS elemental maps. (g), (h), (i), (j) EDS line profiles. (a), (d), (g), (h) Results for the w/o GdOx stack. (g) and (h) are the EDS line profiles observed along to path (1) and (2) in (d), respectively. (b), (e), (i) Results for the w/GdOx [t_{GdOx} =0.6 nm] stack. (c), (f), (j) Results for the w/GdOx [t_{GdOx} =1.2 nm] stack. Note that all the data are obtained from the stacks with $k_{eff}t_{CFB}$ = 1.0 nm.

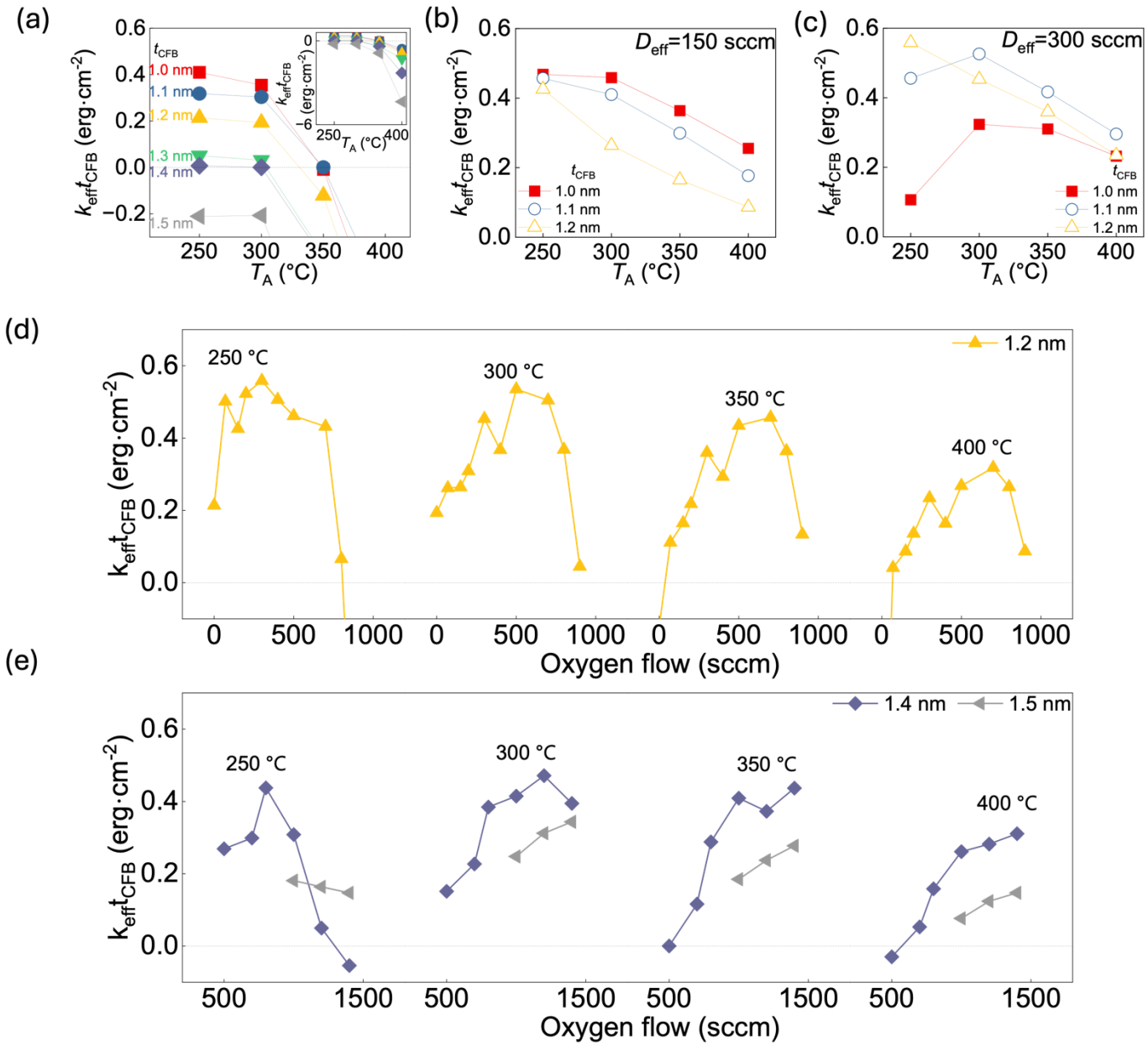

Fig. 4 (a) $k_{eff}t_{CFB}$ as a function of T_A for the w/o GdOx stacks with t_{CFB}=1.0 (squares), 1.1 (circles), 1.2 (up-triangles), 1.3 (down-triangles). 1.4 (diamonds), and 1.5 (left-triangles) nm. Inset presents results with the full scale of $k_{eff}t_{CFB}$.(b), (c) $k_{eff}t_{CFB}$ as a function of T_A for the stacks with t_{CFB}=1.0 (solid squares), 1.1 (open circles), and 1.2 (open triangle). D_{eff} is (b) 150,and (c) 300 sccm. Note that t_{GdOx}=0.2 nm for all the stacks in (b) and (c). (d) $k_{eff}t_{CFB}$ as a function of D_{eff} for several T_as for the stacks with t_{CFB}=1.2 nm and t_{GdOx}=0.2 nm.(e) $k_{eff}t_{CFB}$ as a function of D_{eff} for several T_as for the stacks with t_{CFB}=1.4 nm (diamonds) and t_{CFB}=1.5 nm (triangles). Commonly, t_{GdOx}=0.2 nm for all the stacks. The denoted temperature values in (d) and (e) indicate T_A.

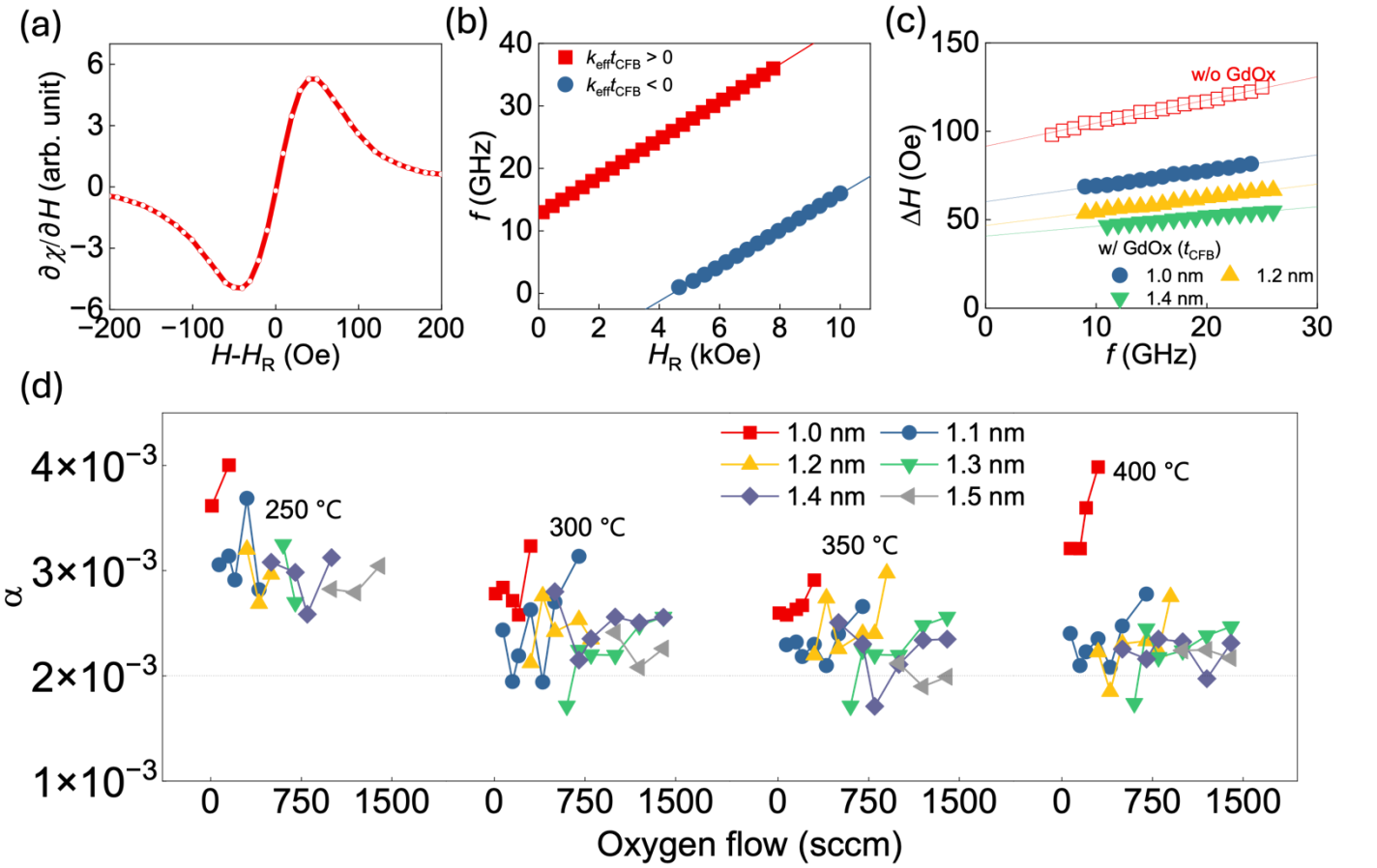

Fig. 5 (a) Typical FMR spectrum from the w/ GdOx (150 sccm) [t_{CFB}=1 nm, t_{GdOx}=0.2 nm, and T_A=350 °C] stack by the application of 15 GHz radiofrequency field. (b) f as a function of H_R. Red and blue symbols for stacks with $k_{eff}t_{CFB} > 0$ [w/ GdOx (9 sccm), t_{CFB}=1 nm, t_{GdOx}=0.2 nm, and T_A=350 °C] and $k_{eff}t_{CFB} < 0$ [w/o GdOx, t_{CFB}=1 nm, and T_A=400 °C] , respectively. (c) ΔH as a function of f. Open red symbols for the w/o GdOx [t_{CFB}=1 nm] stack. Solid red, blue, and yellow symbols for the w/ GdOx stacks with t_{CFB}=1.0 nm [150 sccm], 1.2 nm [500 sccm], and 1.4 nm [800 sccm], respectively. Note that all the stacks presented in (c) are annealed at 350 °C. (d) All observed α for the w/ GdOx stacks as a function of D_{eff}. Here, t_{CFB}=1.0 (squares), 1.1 (circles), 1.2 (up-triangles), 1.3 (down-triangles). 1.4 (diamonds), and 1.5 (left-triangles) nm. Denoted temperature values indicate T_A.

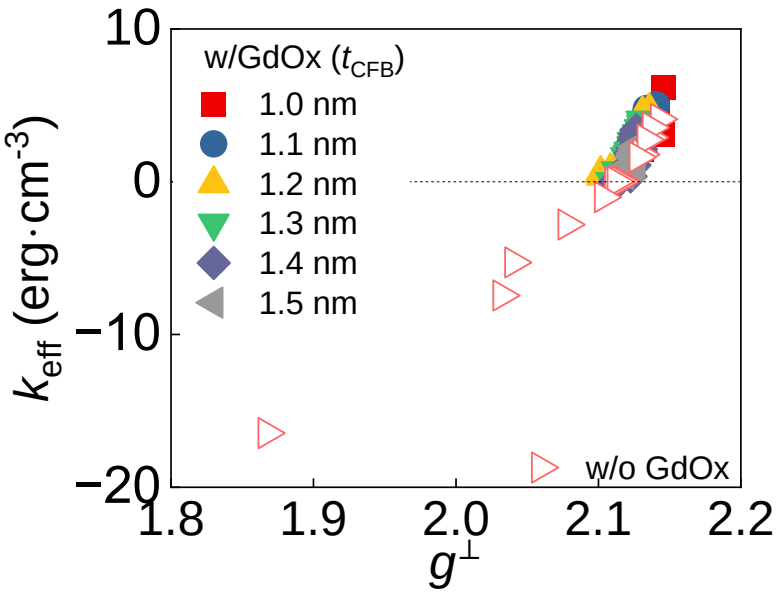

Fig. 6 k_{eff} as a function of $g^{\perp}$ for all the investigated stacks. Open and solid symbols for the w/o GdOx and the w/ GdOx stacks, respectively. t_{CFB} is distinguished by colors and shapes only for the w/ GdOx stacks.